Unraveling the Adsorption Mechanism of Rhodamine B onto Conjugated Polymeric Nanoparticles Using Isothermal Calorimetry and Monte Carlo Simulations

Rodrigo Ponzio, Emmanuel Odella, Elise Prost, Raquel Gutiérrez-Climente, Rodrigo Palacios, Luminita Duma, Carlos Chesta

Unraveling the Adsorption Mechanism of Rhodamine B onto Conjugated Polymeric Nanoparticles using Isothermal Calorimetry and Monte Carlo Simulations

Rodrigo Ponzio,[1] Emmanuel Odella,[1] Elise Prost,[2] Raquel Gutiérrez-Climente,[3] Rodrigo Palacios[1*], Luminita Duma[4*] and Carlos Chesta[1*]

*Corresponding authors: rpalacios@exa.unrc.edu.ar, luminita.duma@univ-reims.fr and cchesta@exa.unrc.edu.ar

[1] *Instituto de Investigaciones en Tecnologías Energéticas y Materiales Avanzados (IITEMA), Universidad Nacional de Río Cuarto-CONICET, Río Cuarto CP5800, Argentina.*

[2] *University of Technology of Compiègne, UPJV, UMR CNRS 7025, Enzyme and Cell Engineering, Research Centre Royallieu, Compiègne, France.*

[3] *EID Méditerranée. 165 avenue Paul Rimbaud, 34184 Montpellier Cedex 4, France.*

[4] *University of Reims Champagne-Ardenne, CNRS, ICMR UMR 7312, 51687, Reims, France*

ABSTRACT

We present herein a comprehensive study on the thermodynamics of rhodamine B (RhB) adsorption onto poly(9,9-dioctylfluorene-alt-benzothiadiazole (F8BT) nanoparticles (NPs) dispersed in water using the isothermal calorimetric titration (ITC) technique. ITC experiments were carried out over a wide temperature range (5-65 °C) and the resulting thermograms were subjected to a detailed thermodynamic analysis using different adsorption models. For this purpose, we developed a versatile computational code based on the Monte Carlo method. We found that the thermograms obtained at the different temperatures cannot be interpreted using the Langmuir, bi-Langmuir or Brunauer, Emmet, Teller (BET) models. However, excellent thermograms fits were attained by applying the Langmuir model coupled with the formation of a RhB dimer on the surface of F8BT NPs. Using this model, the best fit to the experimental data at 25°C yielded the following parameters for direct RhB adsorption on the F8BT NPs surface: equilibrium constant (K_l) of ~ 2x10^7 M^{-1}, enthalpy change (ΔH_l) of ~ 1 kJ mol^{-1} and entropy change

(ΔS_l) of ~ 140 J K^{-1} mol^{-1}. These results indicate that dye adsorption is predominantly an entropy-controlled process. The fit also provided parameters associated with the formation of a second dye adsorption layer, *i.e.*, the formation of the RhB-dimer on the F8BT NPs surface, revealing values of ~1.7 x10^5 M^{-1}, ~ -20 kJ mol^{-1}, and ~ 30 J K^{-1} mol^{-1} for K_m, ΔH_m, and ΔS_m , respectively. The latter two parameters are similar to those previously reported for RhB dimer formation in water (ΔH_d = -12 kJ mol^{-1} and ΔS_d = 22 J K^{-1} mol^{-1}) supporting the chosen Langmuir-dimer model. The analysis of the thermograms also suggests that the NPs surface available for RhB adsorption is small, as compared to the total surface, and that it decreases with decreasing temperature. The latter observation is intriguing, especially since the F8BT NPs hydrodynamic diameter shows only a small decrease with decreasing temperature. To explain these results, we propose that the surface of the NPs harbors highly hydrated polar groups that reduce the accessibility of the dye for adsorption.

INTRODUCTION

In recent years, the use of conjugated polymer nanoparticles (CPNs) has experienced substantial growth in various technological and biomedical fields. Specifically, CPNs have proven to be effective and versatile theragnostic tools in advanced clinical applications, most notably in imaging-based diagnostics and therapies against pathogenic microbial infections [1, 2, 3] and cancer. [4, 5, 6, 7] In particular, CPNs are active materials for the effective application of various therapeutic modalities, such as photodynamic, [8,9] photothermal [10] and sonodynamic therapies. [11] This versatility makes them promising tools for advancing the frontiers of personalized medicine and improving clinical outcomes. CPNs have also been used as photoinitiators of vinyl polymerization in aqueous media, [12,13] allowing the synthesis of hydrogels with a wide variety of clinical applications. [14] In many of these applications, CPNs are deliberately loaded, (either volumetrically or superficially) with synthetic small-molecule dyes to tune their photophysical properties. Particularly, CPNs doped with energy-acceptor dyes have been synthesized and used in a wide variety of applications. In these doped nanomaterials, the polymeric matrix behaves as an antenna that efficiently collects the excitation energy and funnels it to the energy-acceptor dyes. [15,16,17] This antenna effect enhances the excitation of the dye (amplified excitation), allowing a significant improvement in the efficiency of photocatalytic processes, including the generation of

reactive oxygen species (ROS), [18, 19, 20] which is especially important in applications such as cancer phototherapy and bacterial inactivation.

We have previously demonstrated the remarkable capability of F8BT NPs to interact with a broad spectrum of small-molecule dyes, including ionic, zwitterionic and neutral compounds, present in aqueous solutions. [20] More recently, we studied the superficial adsorption of RhB on F8BT NPs, while exploring the CPNs/dye energy transfer mechanism using experimental emission techniques combined with theoretical models and Monte Carlo simulations. [17] We observed evidence that at relatively high dye concentrations RhB forms aggregates on the surface of the CPNs precluding the elucidation of detailed binding thermodynamics using the chosen experimental technique. In related experiments, the interaction between RhB and polymer NPs surfaces has also been examined using NMR spectroscopy. Studies performed by Xu *et al* have shown that saturation-transfer difference (STD) NMR is a reliable method to prove, at the molecular level, the proximity of the aromatic ring of RhB to polystyrene NPs. [21] On a broader context, the binding of substrates to NPs plays a crucial role in the formation of protein coronae when dispersed in biological environments, [22] modulates cell-NPs interactions [23] and affects NPs surface functionalization aimed at conferring specific targeting capabilities. Thus, characterizing the binding model (and associated parameters) for the adsorption of substrates to NPs emerges as a relevant and highly topical challenge. In particular, to study the binding of small molecules to NPs, several spectroscopic analytical techniques, including UV/Vis, [24, 25] FTIR, [26] Raman, [24] and fluorescence, [17, 27, 28] have been extensively used. Depending on the specific system under investigation, these methods can offer qualitative insights into binding and provide essential parameters for quantifying adsorption usually employing the simple Langmuir model. More recently, solution NMR spectroscopy has been applied for detecting and characterizing structure, dynamics, and thermodynamics of surface-bound small molecule species on NPs under optimal conditions. [29] However, a major limitation of this technique is its low sensitivity which limits sample concentration to values between tens of μM to mM, depending on the type of probehead used. This limitation renders therefore difficult an exhaustive exploration of the binding equilibrium over a wide range of relative reagent concentrations. [29].

Isothermal titration calorimetry (ITC) is a straightforward label-free physical method to study binding thermodynamics for a wide range of association reactions such as protein-ligand, [30] protein-protein, [31] protein complexes-DNA, [32] etc.

Association reactions involving small molecules in organic solvents have also been investigated using ITC. [33] In protein-ligand ITC experiments, the ligand (A) is usually titrated into the protein at constant temperature and pressure, while measuring the heat release (Q) of the complexation process. Plotting Q *vs*. the analytical concentration of ligand ($[A]$) generates the experimental binding curve (or thermograms). After that, the thermograms can be subjected to modeling to extract thermodynamic parameters associated with the binding process such as the equilibrium constant, the molar enthalpy and molar entropy changes.

ITC has been also used to quantify the adsorption of proteins (and polymers) on NPs surfaces. [34] Primarily, the interpretation of these adsorption processes has relied on the Langmuir model. Although this simple model has proven suitable in providing a broad understanding of the adsorption phenomena, more complex models are often necessary to accurately capture the nature of protein/NPs binding process. Limitations of the Langmuir model arise from several factors, such as the presence of different types of binding sites for proteins on NP surfaces (bi-Langmuir model), [35] aggregation of proteins on the adsorbent surface (BET-type model) [36, 37, 38] and changes in the tertiary structure of proteins during adsorption. [39] An additional challenge arises from the need to use more complex adsorption models due to an inherent limitation of the ITC technique. ITC thermograms are representations of Q *vs*. $[A]$ rather than Q *vs*. $[A]_f$ (the concentration of the free ligand at the equilibrium), as required by all adsorption models. Unfortunately, when dealing with complex models such as competitive bi-Langmuir, sequential bi-Langmuir and BET, it is impossible to find simple analytical expressions that directly correlate Q with $[A]$. Consequently, there is no straightforward way to obtain thermodynamic information from the thermograms.

To overcome this limitation, we develop a computational code that simulates a series of possible adsorption mechanisms using the Monte Carlo approach. In this case, the thermodynamic parameters of the system are varied over an arbitrary range producing a matrix of simulated data which can then be checked against experimentally measured Q *vs.* $[A]$ curves. Model validation and thermodynamic parameters retrieval of the system are finally achieved by choosing the set of parameters that produces the simulated data that best matches the experimental thermograms. In particular, we applied this combined experimental/theoretical approach to study the thermodynamics of RhB adsorption on

F8BT NPs dispersed in water. By doing so, we identified the adsorption model that best describes the system (Langmuir-dimer) and retrieved its thermodynamic parameters.

MATERIALS AND METHODS

Materials

Poly(9,9-dioctylfluorene-alt-benzothiadiazole) (F8BT, MW = 70,000 g/mol, PDI = 2.4, American Dye Source Inc.) and rhodamine B (RhB, Sigma-Aldrich, 95%) were used as received. Tetrahydrofuran (THF, HPLC grade, Cicarelli) was freshly distilled after being refluxed during 8 h over potassium hydroxide (KOH, pro-analysis grade, Taurus) pellets. Double-distilled water was further purified using an ELGA PURELAB Classic UV system (~18.2 MΩ/cm) to remove ions and organic and particulate matter (0.2 μM filter).

F8BT NPs preparation and characterization

All calorimetry experiments were carried out using an aqueous dispersion of F8BT NPs 83.6 mg/L prepared as follows. 50 mL of a solution of F8BT ~100 mg/L in THF was rapidly poured into 100 mL of deionized water while sonicating. The THF in the mixture and some of the water was later removed under reduced pressure to a final volume of ~40 mL. The resulting NP dispersion was filtered through a polyvinylidene difluoride membrane filter (MilliporeSigma, 0.22 μm pore size) to remove large aggregates and its final volume was brought to 50 mL with water. The concentration of F8BT in the dispersion was calculated using the absorption coefficient of F8BT NPs (42 g^{-1} L cm^{-1} at 455 nm) in water reported previously. [12] The pH of the resulting NPs dispersion was ~6.5.

NPs mean hydrodynamic diameter $\langle d_h \rangle$ measurements were performed with a dynamic light scattering (DLS) instrument (Malvern 4700). Particle suspensions for DLS measurements were filtered through membrane filters (MilliporeSigma, 0.22 μm pore size) right before data acquisition. Three independent measurements were made for each temperature at the scattering angle of 90°. Light scattering results were analyzed with the software provided by the manufacturer (Autosizer 4700) to obtain hydrodynamic diameter distributions by number. The algorithm used for analysis was CONTIN. The average polydispersity index obtained was ≤0.2. The temperature was controlled by a cooling and heating circulating bath (Cole-Parmer) connected to the thermostatizable cell holder. ζ-potential measurements at 25 °C were performed with a Zeta-Sizer Nano ZS90 Instrument. Experiments were carried out in the presence of NaCl 1 mM and results were analyzed with Zetasizer software provided by the manufacturer.

Transmission Electron Microscopy (TEM) images were captured using a JEOL JEM-1400 Flash equipment operating at 120 kV. The TEM sample was prepared by dropwise pouring 50 µL of a 2 mg/L F8BT NPs aqueous dispersion on Formvar/Carbon supported copper grids (Electron Microscopy Sciences) and let it air dry. Analysis of NPs size distribution was performed with ImageJ software, using a total of 15 representative images for evaluation (containing a total of 850 particles).

Calorimetry experiments

Calorimetry experiments were carried-out using a dispersion of F8BT NPs 83.6 mg/L and a solution of RhB 460 µM as titrant. Measurements were performed on a Nano ITC Low Volume (Nano ITC LV) calorimeter from TA Instruments (Waters, France), using a 50 µL injection syringe while stirring at 400 rpm. The equipment contains two gold 170 µL reaction vessels and one burette assembly holding a stainless steel-needle syringe with a twisted paddle at the tip and titrant exit at the bottom. To avoid the formation of bubbles in the cells and the syringe, each solution was degassed for 15 minutes prior to use. For each titration and dilution experiment, the first injection was only initiated after the achievement of baseline stability (using the automatic equilibration mode for "small heats" of ITC run program controlling the calorimeter with the following criteria: absolute acceptable slope: ΔH 0.1 µW/h; acceptable absolute standard deviation: 0.01 µW). In addition, an equilibration time of 3600 s was used before the first injection and 300 s after the last injection to assess the quality of the baseline. The following experimental parameters were employed for carrying out the thermograms at cell temperatures of 5, 25, 45 and 65°C: 350 µL in the sample cell, 50 µL in the syringe, 350 µL solvent in the reference cell, 35 injections of 0.48 µL except for the first injection which was of 0.12 µL meaning that the syringe was not completely emptied at the end of the experiment. A delay of 150 s in between each injection was enough for the baseline to equilibrate. An ITC experiment took between 4 and 5 hours depending on the equilibration duration necessary to fulfill the previously described heat stability criteria. At the beginning and at the end of the series of calorimetric experiments, the sample cell was automatically cleaned with 1 L of 2.5 % DECON followed by 1 L of MilliQ water using the vacuum provided by the degassing device. The verification and validation of the initial manufacturer's criteria are performed thanks to water in water dilution experiments. Three replicates of the titration and dilution experiments with RhB were performed at the different temperatures studied, and results of each series of experiments

were averaged before analysis. The titration integrated heat effects of each injection were corrected by subtraction of the corresponding integrated heat effects associated with RhB dilution into water (Figure 1-SI, SI file). The integration and correction calculations were performed with the software Mathematica 11 which allowed to easily select the corresponding heat peak for each injection.

Python calculations

The simulation code was written in Python language, which is open code and cross platform. The code is parallelized over CPU cores to minimize simulation runtimes. All Python calculations were performed on the supercomputer v2018, based on Sequana X1000 solution from ATOS, of the URCA ROMEO Datacenter (https://romeo.univ-reims.fr/). Python 3.8.3 from anaconda3 has been used to generate the simulated matrix of calorimetric data and the fitting of the ITC data (*vide infra*). The jobs sent to the supercomputer were started with the Slurm workload manager, version 20.11.8-Bull.1.3.

RESULTS AND DISCUSSION

Experimental results

The aqueous F8BT NPs dispersion used in this study was synthesized using the controlled precipitation method as described in Materials and Methods section (Figure 1-A). The size and morphology of NPs were characterized using DLS and TEM, using a dilute particle dispersion (2 mg/L). At 25 °C the average NPs hydrodynamic diameter $\langle d_h \rangle$ is ~43 nm (PDI ~ 0.11, distribution width: σ ~ 3.5 nm) and the corresponding ζ-potential ~ -42.3 mV. F8BT NPs exhibit remarkable stability over long periods of time, which is consistent with their high ζ-potential values. TEM experiments (Figure 1-B) conducted at room temperature revealed a particle size distribution centered around ~50 nm, with a standard deviation (σ) of approximately 10 nm. Figure 1-C (left axis) shows the temperature effect on $\langle d_h \rangle$ as measured by DLS. Considering the experimental uncertainties, it can be concluded that $\langle d_h \rangle$ slightly increases with increasing temperature. Since the adsorption of RhB on the F8BT NPs is an interfacial process, in the same Figure (right axis) the average NPs area $\langle Area \rangle$ is also represented as a function of temperature. As expected, the average area of the NPs distribution calculated as: $\langle Area \rangle = \pi(\langle d_h \rangle^2 + \sigma^2)$ [17] exhibits a similar trend as that observed for $\langle d_h \rangle$.

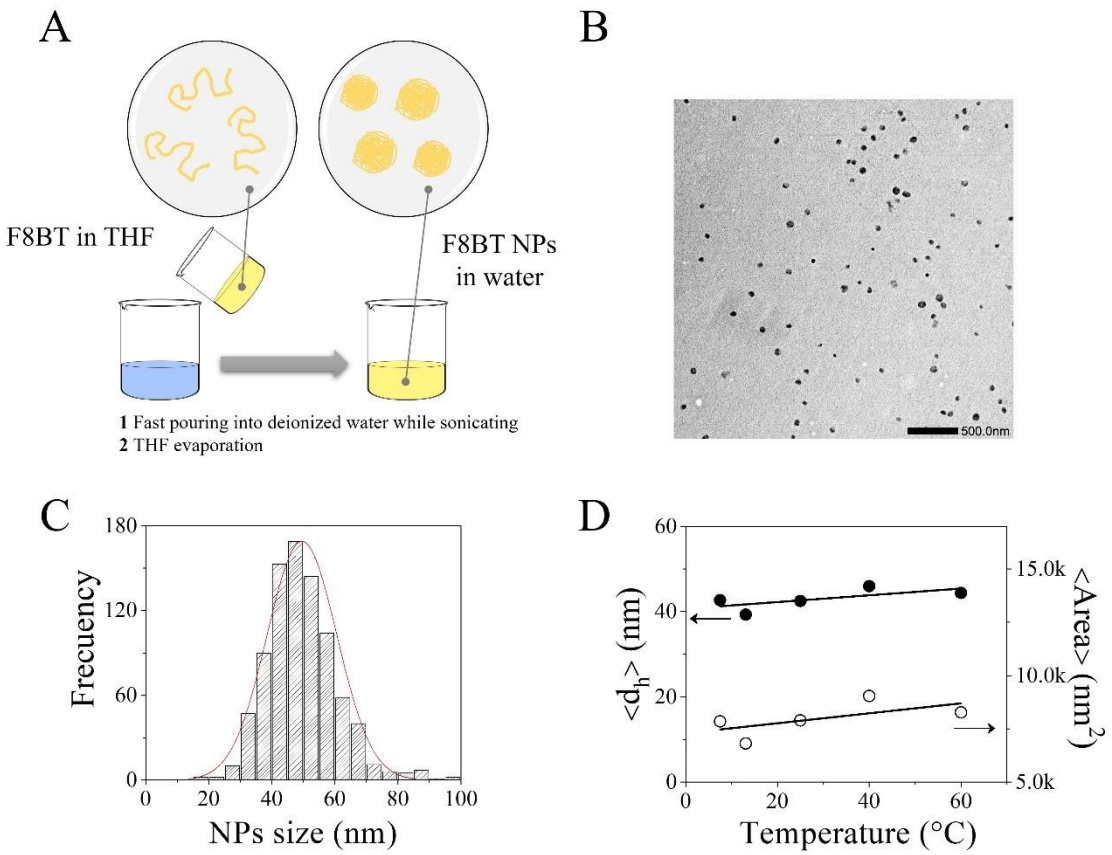

Figure 1: A-Schematic representation of F8BT NPs synthesis. B-Representative TEM micrograph of F8BT NPs. C-F8BT NPs diameter distribution calculated from TEM data. D-Temperature dependence of the average hydrodynamic diameter $\langle d_h \rangle$ of F8BT NPs (left axis) and average NPs superficial area $\langle Area \rangle$ (right axis).

Figure 2-A shows ITC titration curves of F8BT NPs (83.6 mg/L) dispersions with RhB (460 µM) obtained at four temperatures: 5, 25, 45 and 60 °C. Figure 2-B presents the corresponding integrated released heats (Q) as a function of the analytical concentration of RhB (thermograms). Detailed information on these experiments and data processing are given in the Materials and Methods section. As can be seen in Figure 2, titration profiles are highly temperature dependent, showing some similarities but also clear differences. For example, all titration profiles (and thermograms) show two apparent regions: an initial low RhB concentration region displaying very small enthalpic changes and a latter high RhB concentration region where relatively large and negative enthalpic changes are observed. However, the RhB concentration threshold (Figure 2-B) at which the exothermic process becomes apparent increases with increasing temperature.

Interestingly, the comparison of the results at 5 and 25 °C suggests that the exothermic process is completed at relatively low RhB concentrations, and consequently, Q reaches in both cases a plateau (Figure 1-B). At 5 °C, the maximum Q observed is ~ -16 μJ, while at 25 °C, it increases to ~ -30 μJ. In contrast, experiments performed at 45 and 65 °C show that Q continues to increase even above the maximum RhB concentration studied (46 μM), reaching maximum values of ~ -42 μJ and ~ -51 μJ at 45 and 65 °C, respectively. Therefore, it can be concluded that Q increases with increasing temperature. The evidence presented so far, suggests that the thermograms shown in Figure 2-B are the result of at least two processes occurring sequentially. It should be noted that the range of RhB concentrations used in all experiments (0-46 μM) was deliberately chosen to avoid complications associated with the formation of RhB dimers and other species in aqueous solution. As discussed in Section 2-SI, several RhB species can co-exist in aqueous solution depending on the dye concentration, pH, ionic strength and temperature of the medium. However, at concentrations of RhB < 50 μM, it can be safely assumed that the dye exists predominantly in its monomeric zwitterionic form.

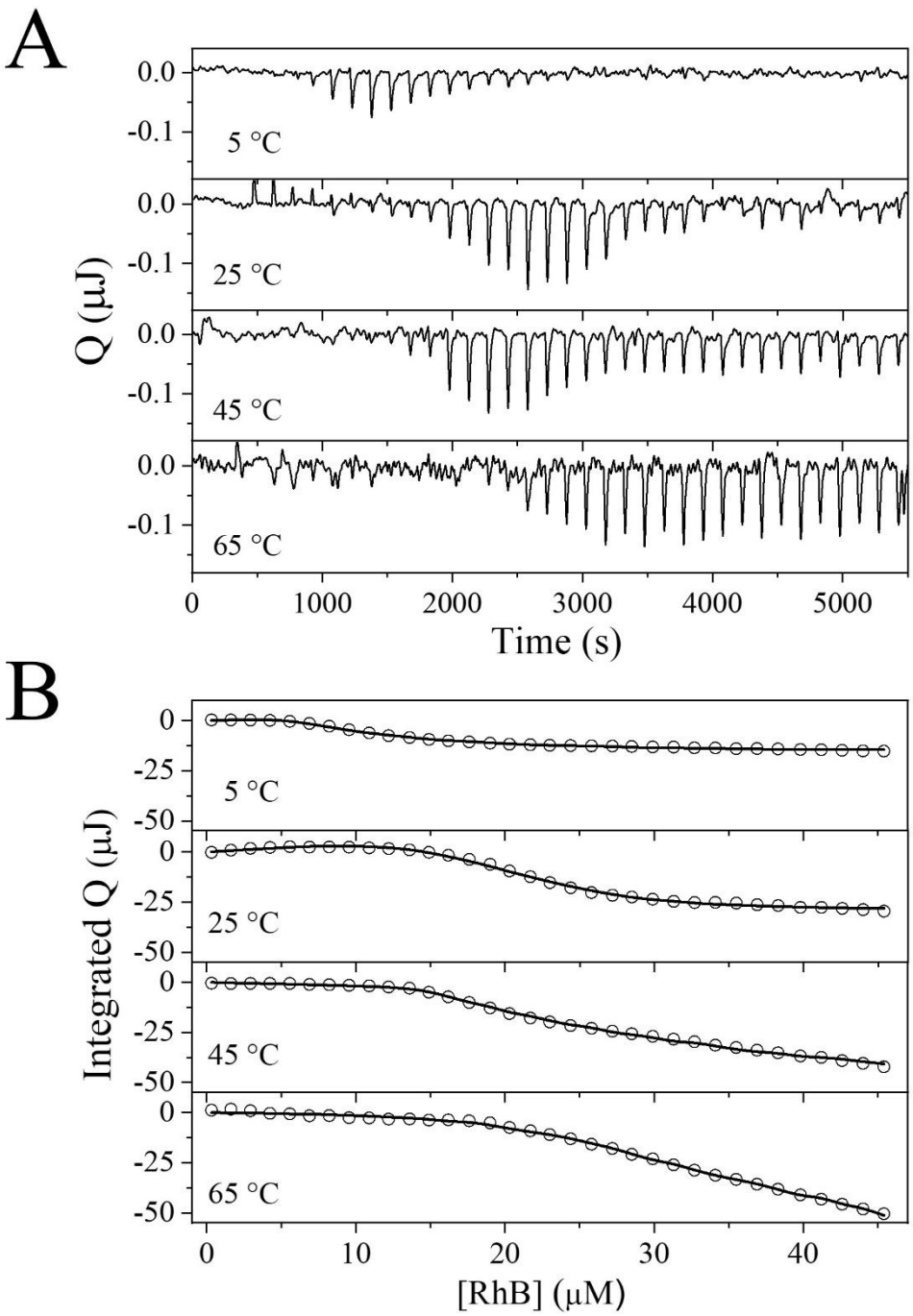

Figure 2: A-ITC titration profiles of aqueous dispersions of F8BT NPs (83.6 mg/L) into RhB (460 μM) corrected by RhB dilution into water. B-Titration thermograms as a function of the analytical concentration of RhB (open circles) and the corresponding fitting to the Langmuir-RhB dimer model (lines).

Interpretation of ITC thermograms using the Langmuir, Langmuir-dimer and BET adsorption models. The well-known Langmuir and BET models were initially developed

for gas-phase equilibrium and were later modified for the adsorption of substrates occurring in liquid-solid interphases. [40,41]. Figure 3 provides a summary of the key parameters considered in the formulation of a BET multilayer adsorption model. The system consists of a solid (sorbent) with a mass m_P, which exposes a set of $m_P N$ identical binding sites for the adsorbate (A), where N represents the moles of sites per gram of sorbent. In this model, the adsorption of A involves two different processes. Initially, A binds to the solid surface and, subsequently, A begins to pile up on top of the initial layer, giving rise to multiple layers. In the same figure, V_c represents the volume of the calorimeter and $[A]_f$ stands for the molar concentration of free (non-bound) A at equilibrium. $[A]_f$ correlates with the A analytical molar concentration ($[A]$) through the following expression: $[A] = [A]_f + [A]_b$, where $[A]_b$ is the molar concentration of total A bound to the absorbent. The relationship between $[A]_b$ and the total moles of A adsorbed into the m_P grams of adsorbent (A_b) is described by: $A_b = [A]_b V_c = A_{bl}^{m_p} + A_{bm}^{m_p}$, where $A_{bl}^{m_p}$ and $A_{bm}^{m_p}$ are the moles A adsorbed on the first (Langmuir) layer and on the successive multilayers, respectively.

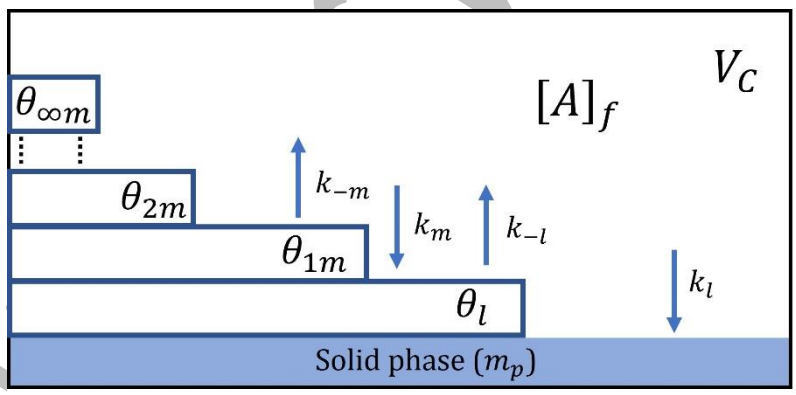

Figure 3: Representation of a multilayer adsorption process.

According to this model, the interaction between a molecule of A and the absorbent surface is characterized by an adsorption equilibrium constant: $K_l = k_l/k_{-l}$; where k_l and k_{-l} are corresponding binding and unbinding rate constants, respectively. Hence, the first (Langmuir-type) layer sites occupancy is defined as: $\theta_l = A_{bl}^{m_p}/m_P N$. On the other hand, A-A interactions leading to multilayer formation over the absorbent surface, are associated to an equilibrium constant: $K_m = k_m/k_{-m}$; where k_m and k_{-m} are corresponding A-A association and dissociation rate constants, respectively. In this

model, K_m is assumed to be identical for all A-stacking processes; *i.e.*, K_m is independent of whether the species formed is a dimer of A (θ_{1m}), a trimer (θ_{2m}), etc. The total number of moles of A forming the multilayer ($A_{bm}^{m_p}$) (*i.e.*, all layers except that directly in contact with the adsorbent) is related to the multilayer degree of occupancy (θ_m) as follows: $\theta_m = \sum_{h=1}^{h=\infty} \theta_{hm} = A_{bm}^{m_p}/m_P N$, where h corresponds to number of multilayers. It should be noted that this definition of θ_m encompasses all adsorption models, since for the Langmuir model simply: $\theta_m = 0$; for the Langmuir-dimer model: $\theta_m = \theta_{1m}$; and for the most general BET model θ_m is the sum over all the layers defined above.

In an ITC experiment, the recorded integrated heat change (Q) is given by:

$$Q = \Delta H_l^0 A_{bl}^{m_p} + \Delta H_m^0 A_{bm}^{m_p} \quad (1)$$

where ΔH_l^0 and ΔH_m^0 are the molar enthalpic changes associated to K_l and K_m, respectively. Considering the definitions of θ_l, θ_m and V_c, equation 1 can be rewritten as:

$$Q = V_c C_P N(\Delta H_l^0 \theta_l + \Delta H_m^0 \theta_m) \quad (2)$$

where $C_P = m_p/V_c$ is the concentration of the adsorbent expressed in g/L. The derivation of the expressions presented thus far is discussed in detail in Section S3-SI. Equation 2 conveniently relates Q values with θ_l and θ_m. However, ITC experiments measure the integrated Q as a function of $[A]$ (see Figure 2-B) instead of $[A]_f$, as required in classical expressions for adsorption isotherms. As demonstrated by Goobes *et al.* [35] and Lindman *et al.* [36], in the case of the Langmuir model (θ_m= 0), a relatively simple expression for θ_l as a function of C_P, N, K_l and $[A]$ can be found, which facilitates a straightforward interpretation of thermograms. In fact, the Langmuir model has been widely used to analyze ITC isotherms, despite the recognition that this model may not always be the most appropriate choice. In more complex scenarios, the interpretation of thermograms involves the separate calculation of θ_l and θ_m as shown in equation 2. However, for the Langmuir-dimer model the expressions for θ_l and θ_m as a function of $[A]$ are quite complicated, making it challenging to apply nonlinear methods to fit these expressions to the experimental thermograms (see section S3-b, SI). Moreover, for the BET model, the derivation of analytical functions for θ_l and θ_m as a function of $[A]$ is not possible.

To address this limitation, we developed a Monte Carlo-based code capable of simulating all types of adsorption models, regardless of their complexity. This code allows us to analyze and extract valuable thermodynamic information from experimental

thermograms represented as a function of $[A]$. This versatility makes the method applicable not only to ITC experiments, but also to any technique (such as absorption, fluorescence, NMR and others) in which the simultaneous and independent determination of $[A]_f$ is not possible or impractical. Although our method requires significant computational effort, it provides a robust phenomenological interpretation of the adsorption process. Moreover, the method can be extended with simple adjustments to encompass all types of adsorption models, serving for the analysis of adsorption kinetics and thermodynamics.

The interpretation of thermograms according to this method involves two stages. Initially, the Monte Carlo-based code simulates (for each adsorption model) a set of θ_l and θ_m *vs.* $[A]$ using an arbitrary matrix of N, K_l and K_m as variable input parameters. Subsequently, the code validates the chosen model and determines all unknown parameters (N, K_l, K_m, ΔH_l^0 and ΔH_m^0) fitting the resulting θ_l and θ_m sets to the experimental thermograms with ΔH_l^0 and ΔH_m^0 serving as adjustable parameters. For this second stage, the multiple linear regression method is employed, where Q represents the dependent variable and θ_l and θ_m the independent ones. Then, the matrix values yielding the best fits are chosen to simultaneously determine the optimal values of N, K_l, K_m, ΔH_l^0 and ΔH_m^0 at each temperature.

Dynamic stochastic simulation of θ using the Monte Carlo method.

Simulation code.

The simulation code was written in Python language, which is open code and cross platform. It is parallelized over CPU cores to minimize simulation runtimes. The method makes several assumptions and requires a number of definitions which are listed and discussed below:

- **Number of sites and adsorbates:** The total number of binding sites and adsorbate molecules in the simulated system are defined as n_S and n_A, respectively. These microscopic variables are related to the macroscopic experimental values C_P, N and $[A]$ according to: $n_A = \frac{[A]}{C_P N} n_S$ (see Section 4-SI for details).
- **Free and bound adsorbates**: The total number of free and bound adsorbates are defined as n_{Af} and n_{Ab}, respectively. Additionally, the total number of A molecules adsorbed directly over the adsorbent and those adsorbed on the

multilayer are defined as n_{Abl} and n_{Abm}, respectively. Considering mass balance, the following relations apply: $n_A = n_{Af} + n_{Ab}$ and $n_{Ab} = n_{Abl} + n_{Abm}$.

- **Sites occupancy:** Using the previous definitions, the degrees of sites occupancy for the first monolayer and the subsequent multilayers are defined as: $\theta_l = n_{Abl}/n_S$ and $\theta_m = n_{Abm}/n_S$, respectively.
- **Site equilibrium constant:** The microscopic (single site) equilibrium constants for direct-adsorbent and multilayer adsorption, are defined as K_{ls} and K_{ms}, respectively. These parameters are calculated from the equivalent ensemble macroscopic ones using the following expressions: $K_{ls} = K_l\left(\frac{C_P N}{n_S}\right)$ and $K_{ms} = K_m\left(\frac{C_P N}{n_S}\right)$.
- **Site rate constants and rates:** The microscopic (single site) desorption rate constants k_{-ls} and k_{-ms} are arbitrarily set to 1 s^{-1}, so that the microscopic adsorption rate constants can be calculated as: $k_{ls} = K_{ls}k_{-ls}$ and $k_{ms} = K_{ms}k_{-ms}$. As it will be discussed below, this assumption does not affect the generality of the method. The microscopic (single site) adsorption (v_{ls} and v_{ms}) and desorption (v_{-ls} and v_{-ms}) rates used in the simulation are calculated as: $v_{ls} = k_{ls}n_{Af}$ and $v_{ms} = k_{ms}n_{Af}$, and: $v_{-ls} = k_{-ls}$ and $v_{-ms} = k_{-ms}$, respectively.
- **Site occupancy**: The number of adsorbed A molecules on a site i is defined as n_{Abi} (site occupancy). Thus n_{Abi} can be 0 or 1 for the Langmuir model; 0, 1 or 2 for the Langmuir-dimer model, or 0, 1, 2, 3, 4, etc., for the BET model. Considering mass balance: $n_{Ab} = \sum_{i=1}^{i=N} n_{Abi}$.
- **Possible site events**: In general, site adsorption/desorption events (e_j) fall into one of the following four categories: adsorption event on an empty site (e_{ls}), desorption event from a site occupied with a single A (e_{-ls}), adsorption event on a site occupied with one or more A (e_{ms}), desorption event on a site occupied with two or more A (e_{-ms}). In particular, the number and type of possible events on any given site i is limited by its starting occupancy and by the chosen model. For the BET model three starting occupancies need to be considered: for $n_{Abi} = 0$, the only possible event is e_{ls}; for $n_{Abi} = 1$, only events e_{-ls} and e_{ms} are possible; and for $n_{Abi} \geq 2$, only events e_{ms} and e_{-ms} are possible. For the Langmuir-dimer model nearly identical considerations are made, except for the starting occupancy $n_{Abi} = 2$ where the only possible event is e_{-ms}. Whereas for the simple Langmuir

model, only two starting conditions need to be considered: $n_{Abi} = 0$, which is identical to the other two models and $n_{Abi} = 1$ where the only possible event is e_{-ls}.

- **Events times**. The (stochastic) time ($t_{i,j}$) it takes for each possible j event to occur in a given i site is computed according to: $t_{i,j} = -\frac{1}{v^{i,j}}\ln(a_{i,j})$, where $a_{i,j}$ is a uniform random number with values between 0 and 1.
- **System state definition**: The microscopic state (configuration) of a model system at any given time is uniquely determined by specifying a complete set of microscopic parameters, *i.e.*: n_s, n_A, K_{ls}, K_{ms}, n_{Abi} (for each site). All other relevant microscopic parameters can be calculated from these values.

Classification of the parameters involved in a typical simulation experiment:

- **Fixed input parameters (derived from experimental measurements):** C_p, V_c, and series of 35 $[A]$ values. As mentioned before these parameters are used to compute n_A, K_{ls} and K_{ms} whereas n_s was set at 100 for practical reasons.
- **Guessed input parameters:** A cubic matrix was constructed containing K_l, K_m, and N values. Matrix intervals were selected to cover a wide range of realistically expected values for each parameter (K_l = 10^6-10^9 M^{-1}, K_m = 10^3-10^8 M^{-1} and N= 10^{-5}-10^{-3} moles of binding sites/g,). For each parameter thirty-five values logarithmically distributed in independent intervals were chosen resulting in a 35x35x35 matrix (42,875 unique combinations of N, K_l and K_m).
- **Output parameters:** simulated θ_l and θ_m *vs.* $[A]$ were obtained for each data point on the previously described matrix.

The following stages take place during a single simulation run yielding kinetic traces of θ_l and θ_m (associated with the state evolution of the system) and the corresponding equilibrium values $\theta_{l,eq}$ and $\theta_{m,eq}$**:**

i. **Setting the initial system state.** At the beginning of the simulation, the absorbent surface is considered to be empty. This implies that at this initial state $n_{Abi} = 0$ for all i, $n_{Ab} = 0$, and $n_{Af} = n_A$.

ii. **Sorting of state fate.** For a given adsorption model and system starting state all possible $t_{i,j}$ are calculated by computing the corresponding $a_{j,i}$. The shortest (or minimum) time (t_{min}) of this set is chosen and the only the event associated with

this particular time is considered to occur. In this way, the fate of all sites is simultaneously sorted (state fate sorting). If t_{min} is associated to an adsorption event occurring in site i, the corresponding n_{Abi} increases by 1 and *vice versa*, while the occupancy of all other sites remains unchanged. Simultaneously the value of n_{Af} decreases or increases by one unit depending on the adsorption/desorption nature of the sorted event. At the end of this cycle, t_{min}, the n_{Abi} of the site whose occupancy was modified, the new n_{Af} and the value of θ_l (and θ_m) are calculated and recorded defining a new system state.

iii. **State fate sorting iteration until convergence is reached.** The cycle described in stage ii is repeated n times until sites occupancy reach equilibrium (or convergence) values $\theta_{l,eq}$ and $\theta_{m,eq}$ (*vide infra*). Figure 4 shows the evolution of θ_l and θ_m as a function of cycle number and time (t) which is defined as: $t = \sum_{k=0}^{k=n} t_{min_k}$, where t_{min_k} is the minimum event time recorded in cycle k. To calculate $\theta_{l,eq}$ and $\theta_{m,eq}$ an arbitrary convergence parameter (σ) was set to 10000. Convergence was thus evaluated by comparing the θ_m value at a given time/cycle ($\theta_m(t_k)$) with the θ_m value σ cycles backwards in the simulation ($\theta_m(t_{k-10000})$). When $\theta_m(t_k) = (\theta_m(t_{k-10000}))$ the simulation run was considered to have converged, and the resulting $\theta_{m,eq}$ is calculated as the average value over the $[\theta_m(t_{k-10000}), \theta_m(t_k)]$ interval.

It is important to note that the magnitude of t is arbitrary, since it depends on the values of k_{ls} and k_{ms}, both chosen as 1 s^{-1} (*vide supra*). However, $\theta_{l,eq}$ and $\theta_{m,eq}$ are independent of rate constants since for a given $[A]$ they depend exclusively on K_l, K_m and N. Figure 4-A represents the initial time/cycle evolution of θ_l and θ_m for a representative simulation run (many cycles). It is important to note that the variable t is not continuous, since it is the cumulative sum of t_{min_k}, whose magnitudes are stochastically calculated as described above. Figure 4-B shows results for the same simulation run as in Figure 4-A but in a longer time scale. The traces in Figure 4-B clearly show that at sufficiently long t (high cycle number) the value of θ_l (black circles) remains quite stable (does not show significant variations). In contrast, simulated θ_m (open circles) values show larger fluctuations associated with a statistical streak effect due to the relatively small value of n_S chosen for the simulations (100 sites). As expected, increasing the number of binding sites decreased the amplitude of fluctuations in the simulated θ values at the expense of longer computing time (data not shown).

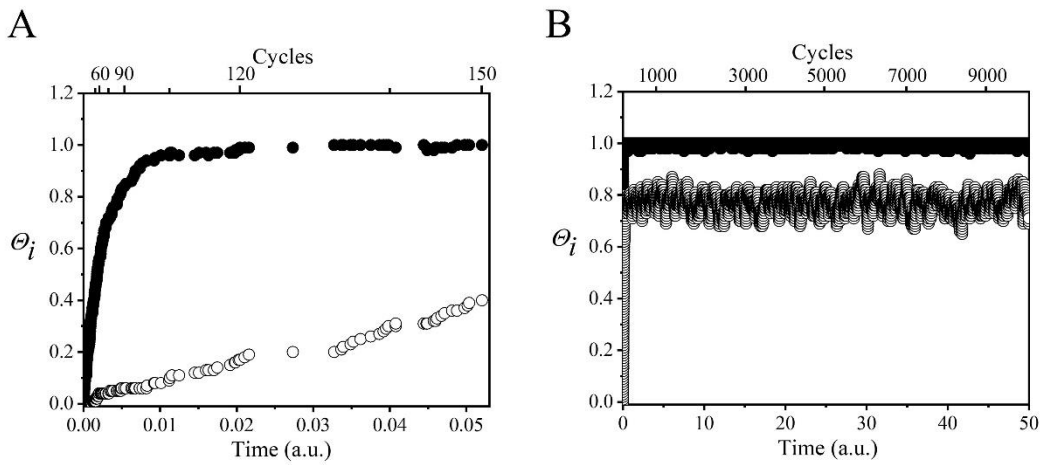

Figure 4: Example of calculated θ as a function of time shown in a short (A) and a long (B) time scale: θ_l (open circles), θ_m (black filled circles). Simulations were performed using a Langmuir-dimer model and the following set of parameters: n_S = 100 sites, K_{ls}= 2.38 molecules^{-1}, K_{ms}= 0.19 molecules^{-1} and n_A = 214 molecules.

Fitting simulation results to the experimental thermograms

Thermograms shown in Figure 1-B were analyzed according to the different adsorption models using the equation 2. Thermograms can be fitted using the multiple linear regression method where Q represents the dependent variable and θ_l and θ_m the independent ones. From such a fit, the values of ΔH_l^0 and ΔH_m^0 can be obtained. However, the set of variables θ_l and θ_m that best fit equation 2 are also unknown, so they must be found simultaneously with the enthalpy change values. That is, the best fit of the thermograms is achieved by finding at once the values of ΔH_l^0, ΔH_m^0, N, K_l and K_m. In addition, while ΔH_l^0 and ΔH_m^0 should be nearly constant within the studied temperature range, N, K_l and K_m are expected to vary for each thermogram. It should be noted that, prior to fitting the experimental data, the validity of the simulation code was confirmed by a comprehensive series of benchmark tests (more details in Section 5, SI). Briefly, for each adsorption model the analytical solution and the simulation results of an arbitrary sample thermographs (Q *vs* $[A]$) were compared yielding identical results within the experimental error associated with the stochastic nature of the simulation (see Figures S5-a, S5-b and S5-c).

Thus, to interpret the thermograms in Figure 1-B we proceeded as follows. The simulated sets of θ_l and θ_m *vs* $[A]$ (calculated employing the N, K_l and K_m matrix) were

fitted to the experimental thermograms using the multiple linear regression method. In other words, each thermogram was fitted with the 42,875 combinations of N, K_l and K_m (*i.e.*: with 42,875 sets of simulated θ_l and θ_m *vs* $[A]$) and the quality of the fit in each case was evaluated using the corresponding R^2. The solid lines in Figure 1-B show the best fits of the thermograms, *i.e.*, the ones showing the highest R^2 value at each temperature (*vide infra*).

As discussed above, the thermograms shown in Figure 1 strongly suggest that RhB adsorption on the F8BT NPs surface occurs through two consecutive stages, so a simple Langmuir or even a (competitive) bi-Langmuir model can be ruled out. Alternative models, such as BET or a (sequential) bi-Langmuir model restricted to RhB dimer formation seems to be more appropriate for thermogram interpretation. As shown in Figure 3 both models assume the adsorption of RhB to form a monolayer on the surface of the NPs, followed by the formation of dimers, trimers or larger RhB aggregates on top of the already occupied surface. It is important to mention that the formation of dimers (or larger dye aggregates) on the surface can start before $\theta_l = 1$. In Figure 5-A, the comparison between the 25°C thermogram fit to the BET and Langmuir-dimer models is shown. The inadequacy of the BET model to properly fit the experimental thermogram is quite evident in contrast with the Langmuir-dimer model, which shows a remarkably good fit. Similar results were observed at all studied temperatures. These results indicate that the formation of RhB dimers is considerably more favorable than the formation of larger aggregates, such as trimers, tetramers, etc., which is in agreement with previous studies in which the formation of RhB trimers in water could be ruled out even at dye concentrations higher than 3.4 10^{-3} M (3400 μM). [42]

Table 1-SI collects the values of ΔH_l^0 and ΔH_m^0, K_l, K_m and N, obtained from the best fits to the experimental thermograms using the Langmuir RhB-dimer model, the corresponding fitting graphs are shown in Figure 2. The temperature dependence of the obtained ΔH_l^0, ΔH_m^0 and N values is shown in Figure 5-B and C, respectively. Van 't Hoff plots constructed from the experimental K_l and K_m are presented in Figure 5-D. Both equilibrium constants are temperature-dependent and exhibit a significant difference in magnitude, with K_l in the order of ~10^7 M^{-1} and K_m in the ~10^5 M^{-1}.

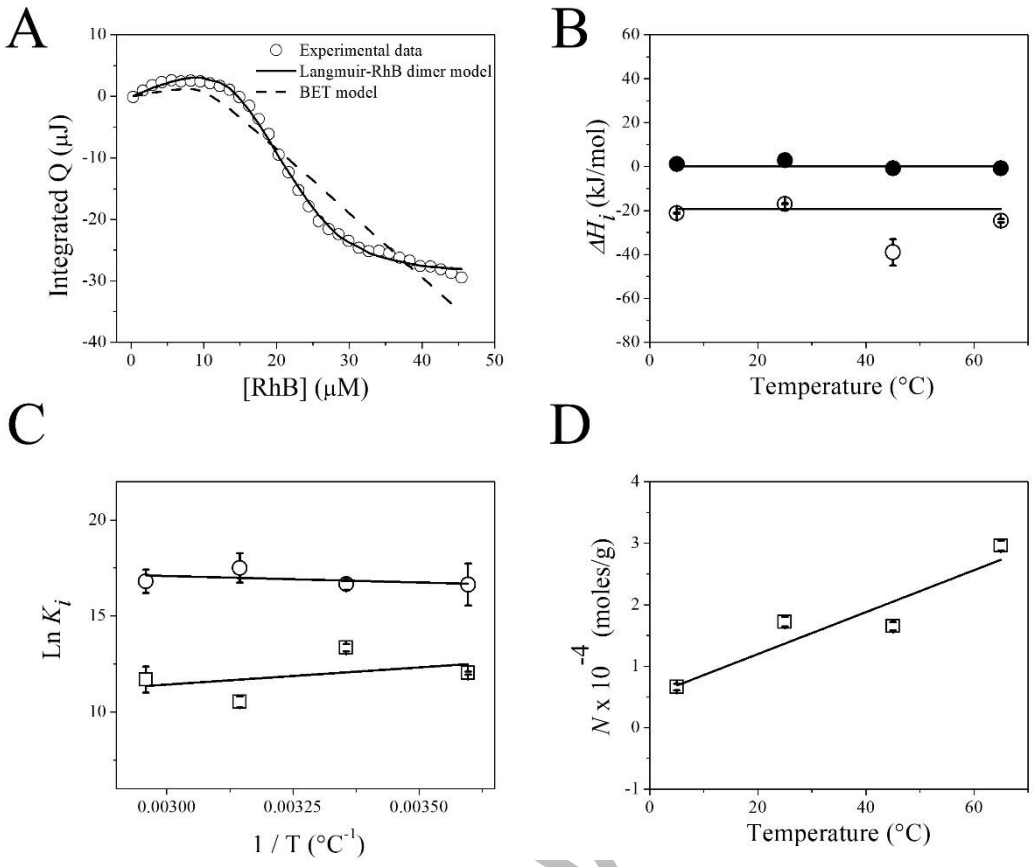

Figure 5: A-Best fit of the experimental thermogram obtained at 25 °C (open circles) using BET (dashed line) and Langmuir-RhB dimer (continuous line) models. B-Experimental ΔH_l^0 and ΔH_m^0 obtained at the different temperatures from thermogram fitting. C- Van 't Hoff plots constructed from the experimental values of K_l (open circles) and K_m (open squares). D- Experimental N as a function of temperature.

As shown in Figure 5-B, within the experimental uncertainties, both ΔH_l^0 and ΔH_m^0 are constant over the explored temperature range. The average (weighted) value of ΔH_l^0 is +(1 ± 2) kJ/mol, while dimer formation process is associated with an enthalpic change of -(20 ± 2) kJ/mol. Figure 5-C shows the values of K_l and K_m as a function of temperature represented according to the Van 't Hoff equation:

$$Ln\ K_i = -\frac{\Delta H_i^0}{RT} + \frac{\Delta S_i^0}{R} \qquad (3)$$

which allows to estimate ΔH_l^0 and ΔH_m^0, as well as the entropic changes associated with the processes: ΔS_l^0 and ΔS_m^0. The results obtained from the linear regression analysis

applied to the plots in Figure 5-C and those directly obtained from thermograms fitting are collected in Table 1.

Table 1: Thermodynamic parameters obtained from the analysis of the thermograms (Figure 1-B) and the Van 't Hoff plots (Figure 5-D). Gibbs free energies and enthalpy changes are given in kJ mol^{-1} and entropy changes in J K^{-1} mol^{-1}.

Thermodynamic parameters	Values obtained from thermogram fitting Figure 1-B	Values obtained from Van 't Hoff analysis Figure 5-C
ΔG_l^0 (25 °C)	- (40.4 ± 0.3) [a]	- (44 ± 10) [b]
ΔH_l^0	+ (1 ± 2)	+ (4 ± 8)
ΔS_l^0	+ (139 ± 6)	+ (160 ± 20)
ΔG_m^0 (25 °C)	- (32.4 ± 0.2) [a]	- (30 ± 40) [b]
ΔH_m^0	- (20 ± 2)	- (20 ± 20)
ΔS_m^0	+ (30 ± 10)	+ (40 ± 80)

[a] Calculated from the values of K_l, K_m, ΔH_l^0 and ΔH_m^0 obtained by fitting the thermogram shown in Figure 5-A. The free energy and entropic changes were estimated as: $\Delta G_i^0 = -RTLnK_i$ and $\Delta S_i^0 = -(\Delta G_i^0 - \Delta H_i^0)/T$, respectively.

[b] Calculated from ΔH_i^0 and ΔS_i^0 obtained from the Van 't Hoff plots (Equation 3).

Examination of Table 1 reveals a good agreement between the values of ΔH_l^0 and ΔH_m^0 obtained by both methods, affirming the robustness of the Langmuir-RhB dimer model employed in the interpretation of the thermograms. The calculated values for ΔH_l^0, ΔS_l^0 (and ΔG_l^0) indicate that the adsorption of RhB on the NPs surface is a spontaneous process, slightly endothermic and mainly controlled by entropy ($T\Delta S_l^0$ ~-42 kJ/mol). This observation implies a weak nonspecific interaction between the polymer surface and the dye. The large positive entropy change observed experimentally for the adsorption process (~140 J K^{-1} mol^{-1}) can in principle be ascribed to the liberation of water molecules that were initially interacting with the F8BT NPs surface and solvating the dye. This phenomenon would largely compensate for the expected negative entropy change due to the immobilization of the dye on the NP surface. Goobes *et al.* [35] reported a comparable

behaviour in their study on the adsorption of staterin on the surface of hydroxyapatite. There is also a good agreement between the values of ΔH_m^0 and ΔS_m^0 calculated for dimer formation using both methods. The formation of this species in water was thoroughly investigated by Rohatgi *et al.* [43] and Selwyn *et al*, [44] covering a range of RhB concentrations from 10^{-6} to 10^{-3} M. Evidence of dimer formation is manifested by the appearance of an intense blue-shifted shoulder in the zwitterionic RhB absorption band around 550 nm. Both authors report similar dimerization equilibrium constant (K_m) of ~7 x 10^3 M^{-1} at room temperature. Rohatgi *et al.* [43] also explored the effect of temperature on the RhB dimer equilibrium, providing values of ~ -12 kJ mol^{-1} and ~+22 J K^{-1} mol^{-1} for ΔH_m^0 and ΔS_m^0, respectively. The authors concluded that the dimerization of RhB in water is also a process mainly governed by entropic factors. The observed gain in entropy was justified by considering that, during aggregation, solvating water molecules are released, causing the non-polar groups of the dye to leave the aqueous medium and cluster to form intermolecular hydrophobic bonds. Similar arguments were used to explain methylene blue dimerization phenomenon in water. [45] It is noteworthy that the value of K_m reported in water is one order of magnitude lower than the one reported here, suggesting that RhB dimer formation is favored on the NPs surface. Although the formation of RhB dimers (and larger aggregates) has been spectrophotometrically detected when the dye is deposited on quartz plates [46] or adsorbed on ZnO, [47] the values of K_m in these systems were not determined, so comparisons are not possible.

As mentioned in the Introduction Section, in previous work from our group, [17] we studied the adsorption of RhB to the surface of F8BT NPs using a fundamentally different approach. An analytical expression derived from the Langmuir model (equation S1, SI file) was fitted to the experimentally measured dye emission anisotropy *vs.* NPs concentration. In these experiments, the adsorption process was explored using very low RhB concentrations (< 40 nM for C_p = 12 mg/L) so as to achieve low θ_l values (< 0.09) and preclude the formation of RhB aggregates. The fitting procedure in this previous work allowed to extract the value of $(NK_l)_{anisotropy}$ ~ 870 L^{-1} g for NPs characterized by a mean surface area of ~2500 nm^2/particle ($\langle Area \rangle_{anisotropy}$). In our current work we obtained N = 1.72x10^{-4} moles/g, K_l =1.7x10^7 M^{-1} and $\langle Area \rangle_{ITC}$ ~ 7900 nm^2/particle. Interestingly, the calculated values of the quotient $\left(\frac{\langle Area \rangle}{NK_l}\right)$ obtained from the previous emission anisotropy measurements (~2.9 x 10^{-12} g m^{-1}) and from the current ITC measurements (~2.8 x 10^{-12} g m^{-1}) are very similar. This remarkable consistency of

material/system parameters obtained using completely independent approaches further validates our chosen model and methodology. Finally, it is noteworthy that since K_l should be independent of NPs size, this result also confirms the proportionality between N and the $\langle Area \rangle$ of the NPs.

As shown in Figure 5-D the number of binding sites on the NPs increases with increasing temperature. Indeed, the value of N nearly quadruples in going from 5 to 65 °C. This significant change not only accounts for the observed increase in the initial delay interval in the thermograms with rising temperature (indicating a higher concentration of RhB needed to fully occupy the NPs surface with higher N) but also explains the rise in the maximum Q value reached during the experiment. With higher N, more dimers can form, leading to a larger maximum heat release throughout the overall process. Since RhB adsorption is an interfacial phenomenon, we initially speculated that this increase of N would be related to the swelling of NPs with increasing temperature. However, as shown in Figure 1-C, the NPs diameter grows only by ~10% over the temperature range studied, which represents an increase of only ~20% of its surface area. Therefore, this diameter increase only partially accounts for the increase of N. An alternative interpretation could be related to the degree of dye coverage of the NPs surface. The maximum number of dyes necessary to achieve complete monolayer cover of the NPs surface (N_{max}) at each studied temperature can be estimated using $\langle Area \rangle$ of the NPs distribution (Figure 1-C) and assuming that one RhB molecule can occupy a surface area of ~1 nm^2. [17, 20] Thus, by comparing these calculated N_{max} with the experimental N, the percentage of NPs surface occupancy ($SO\%$) can be estimated. Following this approach, it can be calculated that $SO\%$ varies between ~10-35% as the temperature increases between 5 and 65 °C. These $SO\%$ values are in fact low, suggesting that dye binding sites occupy only a small fraction of the total NPs area. Interestingly, Lindman et al. [36] reported that the adsorption of human serum albumin (HBA) to NPs prepared from different N-iso-propylacrylamide/ N-tert-butylacrylamide copolymers showed increasing $SO\%$ with decreasing particle surface hydrophilicity. Baier *et al*. [38] obtained comparable results in their investigation of the adsorption of bovine serum albumin (BSA) on NPs derived from methylmethacrylate/acrylic acid and methylmethacrylate/2-aminoethylmethacrylate copolymers. The inclusion of these acidic or basic groups in the polymer structure was used to confer positive or negative charges to the NPs surfaces. The authors showed that adjusting the pH of the NPs dispersion in the range of 3 to 6 led

to a reduction or increase of the NPs surface charge, as evidenced by the variation of NPs ζ-potentials. Interestingly, these authors observed that by reducing the surface charge of both types of NPs (making them less hydrophilic), $SO\%$ was markedly favored, going from ~25 to ~60%. Hence, these results indicate a preference for adsorption of BSA on hydrophobic surfaces, and that the existence of net charges on the NPs surface seems to hinder protein binding. These results can be used to explain the apparent increase in N with increasing temperature observed in this study. As commented above, F8BT NPs are characterized by a large ζ-potential (~ -42.3 mV). Although the origin of the negative charges on the F8BT NPs surface remains unclear, Clafton *et al.* [48] proposed that F8BT undergoes oxidation during the synthesis of the NPs. Accordingly, the polymer recovered from the aqueous NPs dispersion shows the incorporation of oxygen (~12%) and nitrogen (~0.6%), and new IR signals consistent with the formation of -C=O groups. Furthermore, the authors observed that the ζ-potential of NPs decreases as the pH of the dispersion is brought to acidic values, strongly suggesting the presence of acidic groups on their surface. Following Clafton *et al.* [48] and using the experimental values of $\langle d_h \rangle$, $\langle Area \rangle$ and ζ-potential measured at 25°C for the investigated F8BT NPs in this work, we calculated that, on average, a F8BT NPs carry approximately 190 negative charges (at pH~6.5), or in other words, there is one negative charge per ~43 nm^2. Although this surface charge density is not particularly large, these charges play a crucial role in the colloidal stability of the NPs suspension. [49, 50] These charges must be strongly hydrated, forming hydrophilic domains on the surface of the NPs by organizing water molecules at the interface. [51] In the areas not occupied by the hydrated charges there must exist relatively hydrophobic domains where the F8BT/water interactions are significantly smaller, *i.e.*, regions where adsorption of RhB may occur. Therefore, the effect of temperature on N can be explained by considering that the extent of hydrophobic domains increases with increasing temperature. This is supported by the fact that the hydration of anionic groups is an exothermic process [52] and associated with a negative entropy change. Consequently, increasing the temperature of the NPs dispersion would considerably disorganize the solvent water molecules around the surface charges, resulting in an increased probability of the dye reaching the NPs surface and being adsorbed.

CONCLUSIONS

In this study, we used the ITC technique to explore the thermodynamics of RhB adsorption on F8BT NPs dispersed in water. Our investigation covered a wide range of temperatures to elucidate the thermal dependence of the adsorption process. Employing a novel computational code, we analyzed the experimental data using several adsorption models, including: Langmuir, Langmuir coupled to dye dimer formation, and BET models. Our analysis reveals that the Langmuir-dimer model is the one that best fits the experimental data. The results reveal that adsorption of RhB on the surface of F8BT NPs is a spontaneous process, characterized by weak nonspecific interactions between the dye and the polymer and controlled by entropic factors. The significant entropy gains during the process are mostly caused by the displacement of water molecules from the surface of the NPs. This mechanism explains the remarkable ability of F8BT NPs to adsorb various dyes, regardless of their net electric charge, as well as their efficient adsorption on bacterial walls or cell membranes, as demonstrated in our previous studies on photodynamic or sonodynamic therapies. Furthermore, our results indicate that the adsorption of RhB on NPs involves the formation of dye dimers, although no larger aggregates are seen, contrary to what is to be expected by a BET-type model.

Overall, we demonstrate the outstanding capability of ITC measurements combined with computational models based on the Monte Carlo method to unravel complex adsorption mechanisms. We propose that our approach will be especially useful in the study of protein adsorption processes on the surface of NPs or other materials. Moreover, since the developed computational code provides dynamic solutions for the calculation of θ_l and θ_m, it would also allow for the analysis of adsorption kinetics in similar systems. Results of such applications will be reported in the near future by our group.

ASSOCIATED CONTENT

Supporting information

ITC titration profiles and RhB dilution experiments. Discussion on the distribution of RhB species in water. Adsorption models and its application to ITC. Scaling of reagents concentrations and equilibrium constants for simulation using the Monte Carlo method. Benchmark tests for the different simulated adsorption models.

Simulation code

The simulation code written in Python language that allows modeling the adsorption isotherms according to the Langmuir, Longmuir-dimer and BET models is available upon reasonable requests.

AUTHOR INFORMATION

Corresponding Authors

Carlos Chesta − *Instituto de Investigaciones en Tecnologías Energéticas y Materiales Avanzados (IITEMA), Universidad Nacional de Río Cuarto-CONICET, Río Cuarto CP5800, Argentina*.

Email: cchesta@exa.unrc.edu.ar

Luminita Duma − *University of Reims Champagne-Ardenne, CNRS, ICMR UMR 7312, 51687, Reims, France.*

Email: luminita.duma@univ-reims.fr

Rodrigo Palacios − *Instituto de Investigaciones en Tecnologías Energéticas y Materiales Avanzados (IITEMA), Universidad Nacional de Río Cuarto-CONICET, Río Cuarto CP5800, Argentina*.

Email: rpalacios@exa.unrc.edu.ar

Authors

Rodrigo Ponzio − *Instituto de Investigaciones en Tecnologías Energéticas y Materiales Avanzados (IITEMA), Universidad Nacional de Río Cuarto-CONICET, Río Cuarto CP5800, Argentina*.

Emmanuel Odella− *Instituto de Investigaciones en Tecnologías Energéticas y Materiales Avanzados (IITEMA), Universidad Nacional de Río Cuarto-CONICET, Río Cuarto CP5800, Argentina.*

Elise Prost− *University of Technology of Compiègne, UPJV, UMR CNRS 7025, Enzyme and Cell Engineering, Research Centre Royallieu, Compiègne, France.*

Raquel Gutiérrez Climente − *EID Méditerranée. 165 avenue Paul Rimbaud, 34184 Montpellier Cedex 4, France.*

Notes

The authors declare no competing financial interest.

ACKNOWLEDGMENTS

C. C., R. Palacios, R. Ponzio and E.O. are permanent research staff of CONICET-Argentina. The authors appreciate the financial support from the Agencia Nacional de Promoción Científica y Tecnológica (PICT: 2018/2676, 2020/3803, 2021-I-INVI-00589), CONICET (PIP 11220200102377CO01), Ministerio de Ciencia y Tecnología de Córdoba (PICTO-2022-CBA-00065) and Secretaría de Ciencia y Técnica, Universidad Nacional de Río Cuarto, Argentina.

L.D. and E.P. are permanent research staff of CNRS-France. R.G.-C. EID Méditerranée, France. The authors acknowledge financial support from the Hauts-de-France Region and the European Regional Development Fund (ERDF) 2014/2020 for the project BESTMIP (L.D. and R.-G.C.), the Idex Sorbonne Université Investissements d'Avenir (2019/2020 EMERGENCE program), the region Grand Est and the University of Reims Champagne-Ardenne.

TOC Graphic

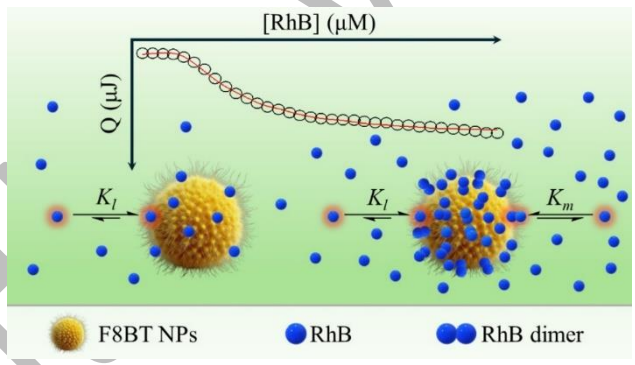

REFERENCES

1- Jiang, J.; Lv, X.; Cheng, H.; Yang, D.; Xu, W.; Hu, Y.; Song, Y.; Zeng, G. Type I Photodynamic Antimicrobial Therapy: Principles, Progress, and Future Perspectives. *Acta Biomater.* **2024**, *177*, 1–19.

2- Ponzio, R. A.; Ibarra, L. E.; Achilli, E. E.; Odella, E.; Chesta, C. A.; Martínez, S. R.; Palacios, R. E. Sweet Light o' Mine: Photothermal and Photodynamic Inactivation of Tenacious Pathogens Using Conjugated Polymers. *J. Photochem. Photobiol. B Biol.* **2022**, *234*, 112510.

3- Martínez, S. R.; Ibarra, L. E.; Ponzio, R. A.; Forcone, M. V.; Wendel, A. B.; Chesta, C. A.; Spesia, M. B.; Palacios, R. E. Photodynamic Inactivation of ESKAPE Group Bacterial Pathogens in Planktonic and Biofilm Cultures Using Metallated Porphyrin-Doped Conjugated Polymer Nanoparticles. *ACS Infect. Dis.* **2020**, *6* (8), 2202–2213.

4- Li, L.; Zhang, X.; Ren, Y.; Yuan, Q.; Wang, Y.; Bao, B.; Li, M.; Tang, Y. Chemiluminescent Conjugated Polymer Nanoparticles for Deep-Tissue Inflammation Imaging and Photodynamic Therapy of Cancer. *J. Am. Chem. Soc.* **2024**, *146* (9), 5927–5939.

5- Ibarra, L. E.; Porcal, G. V.; Macor, L. P.; Ponzio, R. A.; Spada, R. M.; Lorente, C.; Chesta, C. A.; Rivarola, V. A.; Palacios, R. E. Metallated Porphyrin-Doped Conjugated Polymer Nanoparticles for Efficient Photodynamic Therapy of Brain and Colorectal Tumor Cells. *Nanomedicine* **2018**, *13* (6), 605–624.

6- Caverzán, M. D.; Oliveda, P. M.; Beaugé, L.; Palacios, R. E.; Chesta, C. A.; Ibarra, L. E. Metronomic Photodynamic Therapy with Conjugated Polymer Nanoparticles in Glioblastoma Tumor Microenvironment. *Cells* **2023**, *12* (11), 1541.

7- Ibarra, L. E.; Camorani, S.; Agnello, L.; Pedone, E.; Pirone, L.; Chesta, C. A.; Palacios, R. E.; Fedele, M.; Cerchia, L. Selective Photo-Assisted Eradication of Triple-Negative Breast Cancer Cells through Aptamer Decoration of Doped Conjugated Polymer Nanoparticles. *Pharmaceutics* **2022**, *14* (3), 626.

8- Meng, Z.; Hou, W.; Zhou, H.; Zhou, L.; Chen, H.; Wu, C. Therapeutic Considerations and Conjugated Polymer-Based Photosensitizers for Photodynamic Therapy. *Macromol. Rapid Commun.* **2018**, *39* (5), 1–15.

9- Feng, L.; Zhu, C.; Yuan, H.; Liu, L.; Lv, F.; Wang, S. Conjugated Polymer Nanoparticles: Preparation, Properties, Functionalization and Biological Applications. *Chem. Soc. Rev.* **2013**, *42* (16), 6620–6633.

10- Yuan, S.; Zhou, J.; Wang, J.; Ma, X.; Liu, F.; Chen, S.; Fan, J.-X.; Yan, G.-P. Advances of Photothermal Agents with Fluorescence Imaging/Enhancement Ability in the Field of Photothermal Therapy and Diagnosis. *Mol. Pharm.* **2024**, *21* (2), 467–480.

11- Martínez, S. R.; Odella, E.; Ibarra, L. E.; Sosa Lochedino, A.; Wendel, A. B.; Durantini, A. M.; Chesta, C. A.; Palacios, R. E. Conjugated Polymer Nanoparticles as Sonosensitizers in Sono-Inactivation of a Broad Spectrum of Pathogens. *Ultrasonics* **2024**, *137* (July 2023), 107180.

12- Gallastegui, A.; Spada, R. M.; Cagnetta, G.; Ponzio, R. A.; Martínez, S. R.; Previtali, C. M.; Gómez, M. L.; Palacios, R. E.; Chesta, C. A. Conjugated Polymer Nanoparticles

as Unique Coinitiator-Free, Water-Soluble, Visible-Light Photoinitiators of Vinyl Polymerization. *Macromol. Rapid Commun.* **2020**, *41* (8), 1900601.

13- Cagnetta, G. E.; Gallastegui, A.; Martínez, S. R.; Mantione, D.; Criado-Gonzalez, M.; Regato-Herbella, M.; Lezama, L.; Palacios, R. E.; Gómez, M. L.; Mecerreyes, D.; Chesta, C. A. Conjugated Polymer Nanoparticles as Visible Light Panchromatic Photoinitiators for 3D Printing of Acrylic Hydrogels. *Macromolecules* **2024**, *57* (1), 78–87.

14- Cagnetta, G. E.; Martínez, S. R.; Ibarra, L. E.; Gallastegui, A.; Martucci, J. F.; Palacios, R. E.; Chesta, C. A.; Gómez, M. L. Reusable Antimicrobial Antibiotic-Free Dressings Obtained by Photopolymerization. *Biomater. Adv.* **2023**, *149* (November 2022), 213399.

15- Lemmer, U.; Ochse, A.; Deussen, M.; Mahrt, R. F.; Göbel, E. O.; Bassler, H.; Haring Bolivar, P.; Wegmann, G.; Kurz, H. Energy Transfer in Molecularly Doped Conjugated Polymers. *Synth. Met.* **1996**, *78* (3), 289–293.

16- Wu, C.; Zheng, Y.; Szymanski, C.; McNeill, J. Energy Transfer in a Nanoscale Multichromophoric System: Fluorescent Dye-Doped Conjugated Polymer Nanoparticles. *J. Phys. Chem. C* **2008**, *112* (6), 1772–1781.

17- Ponzio, R. A.; Spada, R. M.; Wendel, A. B.; Forcone, M. V.; Stefani, F. D.; Chesta, C. A.; Palacios, R. E. Exciton Diffusion, Antenna Effect, and Quenching Defects in Superficially Dye-Doped Conjugated Polymer Nanoparticles. *J. Phys. Chem. C* **2021**, *125* (42), 23299–23312.

18- Singh, N.; Sen Gupta, R.; Bose, S. A Comprehensive Review on Singlet Oxygen Generation in Nanomaterials and Conjugated Polymers for Photodynamic Therapy in the Treatment of Cancer. *Nanoscale* **2024**, *16* (7), 3243–3268.

19- Shen, X.; He, F.; Wu, J.; Xu, G. Q.; Yao, S. Q.; Xu, Q.-H. Enhanced Two-Photon Singlet Oxygen Generation by Photosensitizer-Doped Conjugated Polymer Nanoparticles. *Langmuir* **2011**, *27* (5), 1739–1744.

20- Spada, R. M.; Macor, L. P.; Hernández, L. I.; Ponzio, R. A.; Ibarra, L. E.; Lorente, C.; Chesta, C. A.; Palacios, R. E. Amplified Singlet Oxygen Generation in Metallated-Porphyrin Doped Conjugated Polymer Nanoparticles. *Dye. Pigment.* **2018**, *149*, 212–223.

21- Xu, H.; Casabianca, L. B. Dual Fluorescence and NMR Study for the Interaction between Xanthene Dyes and Nanoparticles. *Langmuir* **2021**, *37* (1), 385–390.

22- Kopac, T. Protein Corona, Understanding the Nanoparticle–Protein Interactions and Future Perspectives: A Critical Review. *Int. J. Biol. Macromol.* **2021**, *169*, 290–301.

23- Chen, D.; Ganesh, S.; Wang, W.; Amiji, M. Protein Corona-Enabled Systemic Delivery and Targeting of Nanoparticles. *AAPS J.* **2020**, *22* (4), 83.

24- de Haan, M. P.; Balakrishnan, N.; Kuzmyn, A. R.; Li, G.; Willemen, H. M.; Seide, G.; Derksen, G. C. H.; Albada, B.; Zuilhof, H. Alizarin Grafting onto Ultrasmall ZnO Nanoparticles: Mode of Binding, Stability, and Colorant Studies. *Langmuir* **2021**, *37* (4), 1446–1455.

25- Sepideh Kashefi; Lotfollahi, M. N.; Shahrabadi, A. Asphaltene Adsorption Using Nanoparticles with Different Surface Chemistry: Equilibrium and Thermodynamics Studies. *Pet. Chem.* **2019**, *59* (11), 1201–1206.

26- Mudunkotuwa, I. A.; Minshid, A. Al; Grassian, V. H. ATR-FTIR Spectroscopy as a Tool to Probe Surface Adsorption on Nanoparticles at the Liquid–Solid Interface in Environmentally and Biologically Relevant Media. *Analyst* **2014**, *139* (5), 870–881.

27- Pandit, S.; De, M. Interaction of Amino Acids and Graphene Oxide: Trends in Thermodynamic Properties. *J. Phys. Chem. C* **2017**, *121* (1), 600–608.

28- Park, M.; Salem, D. P.; Parviz, D.; Gong, X.; Silmore, K. S.; Lew, T. T. S.; Khong, D. T.; Ang, M. C.-Y.; Kwak, S.-Y.; Chan-Park, M. B.; Strano, M. S. Measuring the Accessible Surface Area within the Nanoparticle Corona Using Molecular Probe Adsorption. *Nano Lett.* **2019**, *19* (11), 7712–7724.

29- An, Y.; Sedinkin, S. L.; Venditti, V. Solution NMR Methods for Structural and Thermodynamic Investigation of Nanoparticle Adsorption Equilibria. *Nanoscale Adv.* **2022**, *4* (12), 2583–2607.

30- Bastos, M.; Abian, O.; Johnson, C. M.; Ferreira-da-Silva, F.; Vega, S.; Jimenez-Alesanco, A.; Ortega-Alarcon, D.; Velazquez-Campoy, A. Isothermal Titration Calorimetry. *Nat. Rev. Methods Prim.* **2023**, *3* (1), 17.

31- Falconer, R. J.; Schuur, B.; Mittermaier, A. K. Applications of Isothermal Titration Calorimetry in Pure and Applied Research from 2016 to 2020. *J. Mol. Recognit.* **2021**, *34* (10), e2901.

32- Gontier, A.; Varela, P. F.; Nemoz, C.; Ropars, V.; Aumont-Nicaise, M.; Desmadril, M.; Charbonnier, J.-B. Measurements of Protein–DNA Complexes Interactions by Isothermal Titration Calorimetry (ITC) and Microscale Thermophoresis (MST); Poterszman, A., Ed.; Springer US: New York, NY, 2021; pp 125–143.

33- Gutiérrez-Climente, R.; Prost, E.; Cordin, A.; Chesta, C.; Duma, L. Isothermal Calorimetry: Molecular Interactions between Small Molecules in Organic Solvents. In

Applications of Calorimetry; Rivera-Armenta, J. L., Flores-Hernández, C. G., Eds.; IntechOpen: Rijeka, 2022.

34- Prozeller, D.; Morsbach, S.; Landfester, K. Isothermal Titration Calorimetry as a Complementary Method for Investigating Nanoparticle–Protein Interactions. *Nanoscale* **2019**, *11* (41), 19265–19273.

35- Goobes, R.; Goobes, G.; Campbell, C. T.; Stayton, P. S. Thermodynamics of Statherin Adsorption onto Hydroxyapatite. *Biochemistry* **2006**, *45* (17), 5576–5586.

36- Lindman, S.; Lynch, I.; Thulin, E.; Nilsson, H.; Dawson, K. A.; Linse, S. Systematic Investigation of the Thermodynamics of HSA Adsorption to N-Iso-Propylacrylamide/N-Tert-Butylacrylamide Copolymer Nanoparticles. Effects of Particle Size and Hydrophobicity. *Nano Lett.* **2007**, *7* (4), 914–920.

37- Eren, N. M.; Narsimhan, G.; Campanella, O. H. Protein Adsorption Induced Bridging Flocculation: The Dominant Entropic Pathway for Nano-Bio Complexation. *Nanoscale* **2016**, *8* (6), 3326–3336.

38- Baier, G.; Costa, C.; Zeller, A.; Baumann, D.; Sayer, C.; Araujo, P. H. H.; Mailänder, V.; Musyanovych, A.; Landfester, K. BSA Adsorption on Differently Charged Polystyrene Nanoparticles Using Isothermal Titration Calorimetry and the Influence on Cellular Uptake. *Macromol. Biosci.* **2011**, *11* (5), 628–638.

39- Latour, R. A. The Langmuir Isotherm: A Commonly Applied but Misleading Approach for the Analysis of Protein Adsorption Behavior. *J. Biomed. Mater. Res. Part A* **2015**, *103* (3), 949–958.

40- Ebadi, A.; Soltan Mohammadzadeh, J. S.; Khudiev, A. What Is the Correct Form of BET Isotherm for Modeling Liquid Phase Adsorption? *Adsorption* **2009**, *15* (1), 65–73.

41- Marbán, G. BET Adsorption Reaction Model Based on the Pseudo Steady-State Hypothesis for Describing the Kinetics of Adsorption in Liquid Phase. *J. Colloid Interface Sci.* **2016**, *467*, 170–179.

42- Arbeloa, F. L.; Ojeda, P. R.; Arbeloa, I. L. Flourescence Self-Quenching of the Molecular Forms of Rhodamine B in Aqueous and Ethanolic Solutions. *J. Lumin.* **1989**, *44* (1–2), 105–112.

43- Rohatgi, K. K.; Singhal, G. S. Nature of Bonding in Dye Aggregates. *J. Phys. Chem.* **1966**, *70* (6), 1695–1701.

44- Selwyn, J. E.; Steinfeld, J. I. Aggregation of Equilibriums of Xanthene Dyes. *J. Phys. Chem.* **1972**, *76* (5), 762–774.

45- Mukerjee, P.; Ghosh, A. K. The Effect of Urea on Methylene Blue, Its Self-Association, and Interaction with Polyelectrolytes in Aqueous Solution. *J. Phys. Chem.* **1963**, *67* (1), 193–197.

46- Kemnitz, K.; Tamai, N.; Yamazaki, I.; Nakashima, N.; Yoshihara, K. Fluorescence Decays and Spectral Properties of Rhodamine B in Submono-, Mono-, and Multilayer Systems. *J. Phys. Chem.* **1986**, *90* (21), 5094–5101.

47- Spitler, M.; Calvin, M. Adsorption and Oxidation of Rhodamine B at ZnO Electrodes. *J. Chem. Phys.* **1977**, *67* (11), 5193–5200.

48- Clafton, S. N.; Beattie, D. A.; Mierczynska-Vasilev, A.; Acres, R. G.; Morgan, A. C.; Kee, T. W. Chemical Defects in the Highly Fluorescent Conjugated Polymer Dots. *Langmuir* **2010**, *26* (23), 17785–17789.

49- Israelachvili, J. N. *Intermolecular and Surface Forces*; Academic Press, 2011.

50- Lunardi, C. N.; Gomes, A. J.; Rocha, F. S.; De Tommaso, J.; Patience, G. S. Experimental Methods in Chemical Engineering: Zeta Potential. *Can. J. Chem. Eng.* **2021**, *99* (3), 627–639.

51- Fenter, P.; Lee, S. S. Hydration Layer Structure at Solid–Water Interfaces. *MRS Bull.* **2014**, *39* (12), 1056–1061.

52- Merdaw, A. A.; Sharif, A. O.; Derwish, G. A. W. Mass Transfer in Pressure-Driven Membrane Separation Processes, Part II. *Chem. Eng. J.* **2011**, *168* (1), 229–240.